# Decoupling and Coupling of the Host-to-Dopant Interaction by Manipulating Dopant Movement in Core/Shell Quantum Dots

Elan Hofman,  $^{\dagger}$  Alex Khammang,  $^{\ddagger}$  Joshua T. Wright,  $^{\#}$  Zhi-Jun Li,  $^{\dagger}$  Peter Francis McLaughlin,  $^{\dagger}$  Andrew Hunter Davis,  $^{\dagger}$  Arindam Chakraborty,  $^{*\dagger}$  Robert W. Meulenberg,  $^{*\dagger}$  Weiwei Zheng  $^{*\dagger}$ 

# **KEYWORDS**

Doped core/shell quantum dots, dopant migration, dopant ejection, host-dopant coupling, energy transfer

# **ABSTRACT**

Doping through the incorporation of transition metal ions allows for the emergence of new optical, electrical, and magnetic properties in nanocrystals (NCs). The properties of doped nanocrystals are largely controlled by the wavefunction overlap between host lattice and dopant ions, i.e. the host-dopant (H-D) coupling. However, it is challenging to fine-tune the H-D coupling of doped NCs after dopant incorporation inside NCs. In this work, we have studied dopant behaviors in Mn:CdS/ZnS core/shell quantum dots (QDs) in a wide temperature range (120 - 300 °C) and found that dopant transport at the nanoscale is very sensitive to factors such as the temperature and microenvironments within the QDs, including interfacial alloys and composition gradients. In addition to the partial loss of surface dopants during initial ZnS shell passivation of Mn(II)-doped CdS QDs, we have identified two well-defined behaviors of incorporated Mn dopants: directional dopant diffusion (i.e. migration) and ejection separated by a temperature boundary (T<sub>b</sub>) at ~200 °C within CdS/ZnS core/shell QDs. Mn migration toward the alloyed interface, below T<sub>b</sub>, weakens the H-D interactions. At temperatures higher than the T<sub>b</sub>, however, dopant ejection and global alloying of CdS/ZnS QDs can occur, leading to stronger H-D coupling. Therefore, the H-D interaction in Mn doped CdS/ZnS QDs can be decoupled and coupled by manipulating dopant movement and local composition of host lattice for continuously tunable optical properties. The behavior of incorporated dopants inside QDs is fundamentally important for understanding doping mechanisms and the host-dopant interactiondependent properties of doped nanomaterials.

# Introduction

Incorporation of transition metal ions as dopants into semiconductor quantum dots (QDs) can introduce new optical, electronic, and magnetic properties,<sup>1-11</sup> making the doped QDs valuable components for applications in light emitting devices, bioimaging, solar cells, and spintronics.<sup>12-16</sup> The properties of doped QDs are strongly influenced by the dopant sites (*i.e.* surface, core, or specific depth from the surface) inside the QDs,<sup>17-21</sup> which determines the host-dopant (H-D) coupling from the overlap between the dopant and exciton wavefunctions of the host lattice.<sup>5</sup> Tuning the H-D coupling by controlling the dopant sites after incorporation in the host lattice, however, is challenging.

In the past two decades, many synthetic methodologies have been developed for introducing dopants inside QDs. Successful doping by dopant incorporation up to its solubility limit can be achieved by a pre-doped single source precursor, 7-8, 22 nucleation doping, 23-24 growth doping, 17, 25-27 as well as ion exchange and diffusion. 3, 28-30 Despite significant developments in the synthesis of doped QDs, limited study has been done on the mass transport behaviors of dopants as well as the change in the microenvironment of the host lattice after dopant incorporation inside QDs, 31-33 or toward a mechanistic understanding of dopant behavior in the host core/shell lattice.

<sup>†</sup> Department of Chemistry, Syracuse University, Syracuse, New York 13244, United States

<sup>&</sup>lt;sup>‡</sup> Department of Physics and Astronomy and Frontier Institute for Research in Sensor Technologies, University of Maine, Orono, Maine 04469, United States

<sup>&</sup>lt;sup>#</sup> Department of Physics, Illinois Institute of Technology, Chicago, Illinois 60616, United States

In this work, we prepared Mn:CdS/ZnS core/shell QDs utilizing a highly reactive zinc and sulfur containing precursor, zinc diethyldithiocarbamate (Zn(DDTC)<sub>2</sub>, for ZnS shell growth (Figure 1a). The Zn(DDTC)<sub>2</sub> precursor is thermally unstable at temperatures as low as 100 °C in the presence of amines, 34 which can rapidly decompose and condenses onto the Mn:CdS QDs to form Mn:CdS/ZnS core/shell QDs. This single source shelling precursor (SSSP) method allows us to monitor the mass transport of both host cations and dopants in a wider temperature range (120 °C to 300 °C in this study) compared with the typical successive ionic layer adsorption and reaction (SILAR) method for shell coating. Three distinct stages are observed during the shelling process including: I) surface dopant replacement during the initial ZnS passivation; II) dopant migration toward the alloyed interface of CdS/ZnS core/shell QDs; and III) global alloying of host QDs and dopant ejection above a temperature boundary (T<sub>b</sub>, ~200 °C). We found that dopant behavior is highly dependent upon the internal composition of the host QDs, primarily related to the presence/extent of alloying (alloyed interface or globally alloyed QDs), and temperature. Specifically, dopant migration toward the alloyed interface (Cd<sub>1-x</sub>Zn<sub>x</sub>S) of the core/shell QDs, decreasing H-D coupling, can be initiated by the availability of dopant sites with smaller cationic size mismatch inside the QDs below a temperature boundary (T<sub>b</sub>, ~200 °C). Above T<sub>b</sub>, however, dopant ejection can occur accompanied by global alloying of QDs. Surprisingly, re-strengthened H-D coupling was observed even with a decreased doping concentration, which could be understood as the nearly flat band alignment of the globally alloyed of QDs. The temperature- and lattice micro-composition-dependent dopant behaviors provide new ways to fine tune the dopant arrangement inside QDs and consequently the properties of doped QDs. Thermodynamic behavior of an incorporated dopant inside a QD is fundamentally important for understanding doping mechanisms and host-dopant interactions.

# Results

**Micro-composition of Mn:CdS/ZnS core/shell QDs.** Mn:CdS QDs were synthesized through a colloidal hotinjection method, as previously reported. <sup>19</sup> The Mn:CdS QDs of 3.0 nm average size (Figure 1b) are in the zinc blend phase based on the X-ray diffraction (XRD) pattern (Figure 1e). To monitor the structural and composition changes of the host core/shell QDs in a wide temperature range, we synthesized ZnS shell passivated Mn:CdS QDs (i.e., Mn:CdS/ZnS core/shell QDs) using a SSSP method by heating Zn(DDTC)<sub>2</sub> with purified Mn:CdS QDs from 120 °C to 300 °C (See details in Supporting Information). The Zn(DDTC)<sub>2</sub> precursor rapidly decomposed above 100 °C in the presence of oleylamine and condensed onto the Mn:CdS QDs to form Mn:CdS/ZnS core/shell QDs. The size of the core/shell QDs increases gradually with the diameters of the core/shell QDs being  $3.8 \pm 0.3$ ,  $4.6 \pm 0.3$ ,  $5.1 \pm 0.4$ , and  $5.5 \pm 0.5$  nm at 120, 160, 200, and 260 °C, respectively (Figure 1c, 1d and Figure S1 and S2). The size of the core/shell QDs remains constant for the proceeding reaction period (260 - 300 °C).

During the ZnS shell growth, a clear shift of the XRD peaks toward zinc blend phase ZnS was observed in Mn:CdS/ZnS QDs (Figure 1e, 1f and Figure S3). As the temperature increased, the diffraction peaks experience a systematic shift to higher angles until 200 °C, followed by a small shift to lower angles with increasing temperature (Figure 1f and Figure S3b). The diffraction peaks shifting to lower angles indicates the formation of globally alloyed QDs (Cd<sub>1-x</sub>Zn<sub>x</sub>S) with intermediate lattice parameters (Table S1), as the result of high temperature annealing (> 200 °C).

To further probe the temperature-dependent composition variation within the Mn:CdS/ZnS core/shell QDs, X-ray absorption fine structure (XAFS) measurements were conducted to study the atomic bonding parameters of the QDs. The Zn K-edge X-ray absorption near edge structure (XANES) consistently decreases in intensity as a function of temperature (Figure 1g, Figure S4 and Table S2), suggesting substitution of larger Cd atom into the ZnS lattice, which is consistent with Zn K-edge XANES simulations (Figure S5). The fitting of the extended XAFS (EXAFS) data (Figure S4) show an immediate increase in Zn-S bond length during shell passivation (Figure 1i), which is consistent with the incorporation of surface Cd cations from the CdS core into the ZnS lattice, as expected for the formation of the alloyed surface/interface (T < temperature boundary (T<sub>b</sub>, ~200 °C), and alloyed QDs (T > T<sub>b</sub>) (Figure 2a insert). The Cd-S bond length, however, from the Cd K-edge EXAFS fitting (Figure S6 and Table S2) does not initially change and only exhibits a significant shift of the Cd K-edge XANES onset (Figure 1h) above T<sub>b</sub>. This is due to the CdS core being largely undisturbed with only a small fraction of the surface Cd actually alloying with Zn to form the alloyed interface below T<sub>b</sub>. Above T<sub>b</sub>, the Cd K-edge XANES shifts to lower energy (ca. 1 eV) and the Cd-S bond length gradually decreases, which is consistent with a complete

alloy transformation as suggested from the XRD (Figure 1f and 1h, Table S1). We do note that Mn K-edge XAFS measurements were also attempted, but due to the low Mn doping concentration, appreciable X-ray absorption edge jumps were on the order of ~0.005, and therefore it was not possible to observe any useful signal.

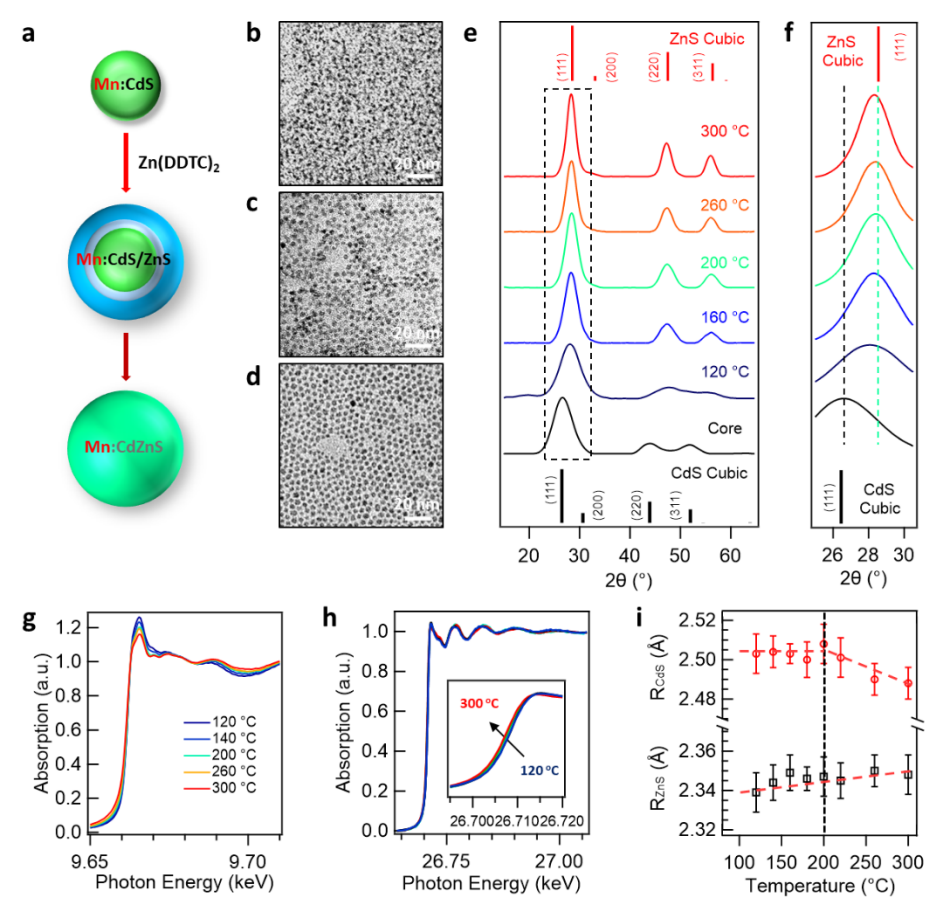


**Figure 1**. Size, structural, and micro-composition Mn:CdS/ZnS core/shell QDs. (a) Schematic illustration of the SSSP method for the composition variation of Mn:CdS/ZnS QDs during ZnS shell passivation. (b-d), TEM images of Mn:CdS core and selective Mn:CdS/ZnS core/shell (200 and 300 °C) QDs; (e) Powder XRD patterns of Mn:CdS core and selective Mn:CdS/ZnS core/shell QDs (120, 160, 200, 260, 300 °C); (f) zoomed-in XRD patterns of the (111) diffraction peak; (g) Zn K-edge XANES and (h) Cd K-edge XANES for Mn:CdS/ZnS QDs as a function of temperature; (i) Cd-S and Zn-S bond lengths as obtained from EXAFS fits versus temperature.

Temperature and host micro-composition dependent dopant behaviors in CdS/ZnS QDs. Inductively coupled plasma-optical emission spectrometry (ICP-OES) measurements indicate 1.4% Mn doping concentration (calculated as a ratio of Mn/(Cd + Mn), Table S3) for Mn:CdS QDs (Figure 2a). The Mn(II) ions exhibit a Poisson distribution within the QD ensemble, but on average represents ~7 Mn(II) ions distributed stochastically between the core and surface per 3.0 nm Mn:CdS QD. Two sets of electron paramagnetic resonance (EPR) hyperfine splitting patterns were observed in the Mn:CdS QDs with hyperfine constants (A) equaling 69.1 and 94.0 G (Figure 2b and Figure S6), which are attributed to Mn(II) located within the core lattice and on the QD surface, respectively. 35-36 In addition, a broad dipolar background of the EPR indicates the presence of short-range Mn–Mn interactions in the CdS QDs. 37

The Mn(II) concentration decreases to 0.9% after the growth of the ZnS shell at 120 °C (Stage I: initial surface dopant replacement) and remains unchanged for core/shell QDs grown up to 260 °C (Figure 2a), indicating partial surface dopant removal during the initial shell coating process, which is consistent with previous reports. <sup>17,38</sup> The Mn(II) concentration decreases to 0.6% for the core/shell QDs grown at 300 °C (Figure 2a), indicating dopant ejection at high temperatures.

During ZnS shell passivation, both the dipolar term and the surface hyperfine in EPR spectra are largely quenched resulting in the presence of a single core hyperfine term (A = 69.1 G) at high temperatures (Figure 2b and Figure S7). A weaker dipolar contribution in EPR for the QDs grown at 120 °C can still be observed. However, decreased dipolar contribution from 120 to 160 °C (and above) during ZnS shell passivation, indicates larger Mn–Mn distances caused by dopant ion migration,<sup>37</sup> considering the same doping concentration in those QDs.

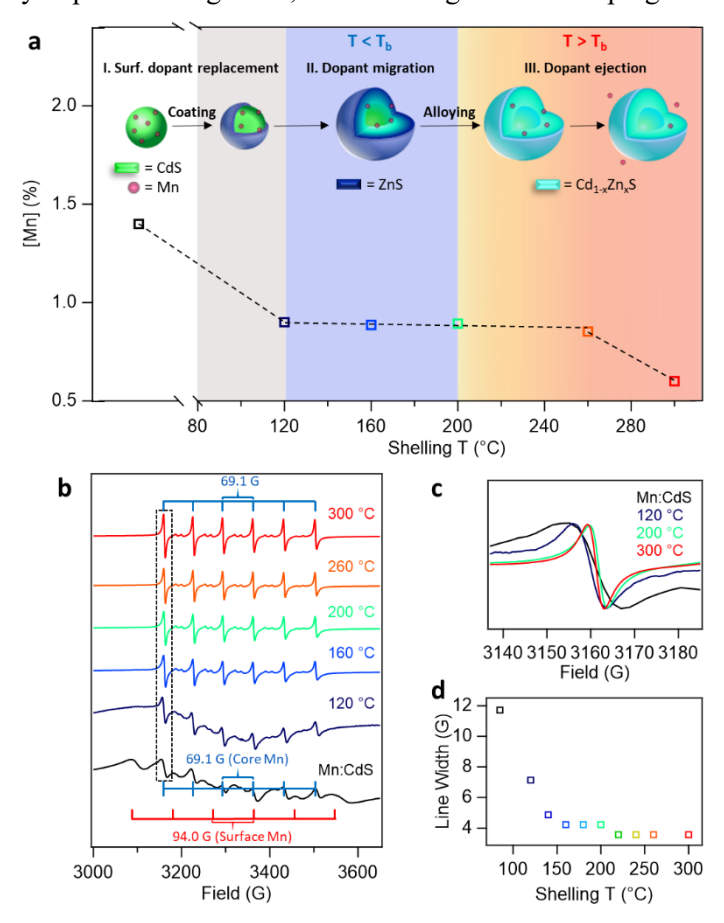


**Figure 2**. Three different dopant behaviors with different dopant concentrations and doping environments during ZnS shell passivation at different temperatures. (a) Mn doping concentration in Mn:CdS core and Mn:CdS/ZnS core/shell QDs throughout the shelling process. The inset on top of Figure 2a shows the temperature-dependent dopant replacement (Stage I), migration (Stage II), and ejection (Stage III) during ZnS shell passivation; (b) Room-temperature X-band EPR spectra of Mn:CdS core and Mn:CdS/ZnS core/shell QDs (a). Two discrete sites for the Mn(II) occupying a substitutional Cd(II) site within the core ( $A_{core} = 69.1$  G) and surface ( $A_{surface} = 94.0$  G) are labeled for the Mn:CdS QDs. Only the Mn core site ( $A_{core} = 69.1$  G) is observed for Mn:CdS/ZnS core/shell QDs grown at temperatures above 120 °C. (c) Zoomed-in view of the first peak of the Mn core EPR signal from (b); (d) the linewidth of the first peak of the core Mn EPR signal during the ZnS shell passivation.

In addition, the linewidth of the Mn EPR hyperfine peak during ZnS shell passivation continually narrowed from 11.7 G for Mn:CdS QDs to 3.6 G for the doped globally alloyed CdZnS QDs grown at 300 °C (Figure 2c and 2d). The narrower EPR peak line-width indicates weaker Mn–Mn interactions and less local strain on the Mn(II) dopant sites. For the Mn incorporation inside CdS QDs, large strain can occur due to the 13% cationic size mismatch between Cd(II) and Mn(II) ions, as well as additional strain from the 7% lattice mismatch between the CdS and ZnS in the Mn:CdS/ZnS core/shell QDs. The strain can introduce an anisotropic distortion of the Mn ligand coordinating environment, leading to a broad Mn EPR peak linewidth. However, considering the size of Mn(II) ions (80 pm) as an intermediate between that of Cd(II) (92 pm) and Zn(II) (74 pm), 19, 38, 40 smaller strain could be obtained from the Mn doped CdZnS alloyed lattice compared with Mn:CdS QDs. Therefore, the alloyed lattice can more readily accommodate Mn ions 38 and Mn migration towards the CdZnS alloyed interface (Stage III) or globally CdZnS alloyed QDs (Stage III) is thermodynamically favored. The smaller strain on the Mn in

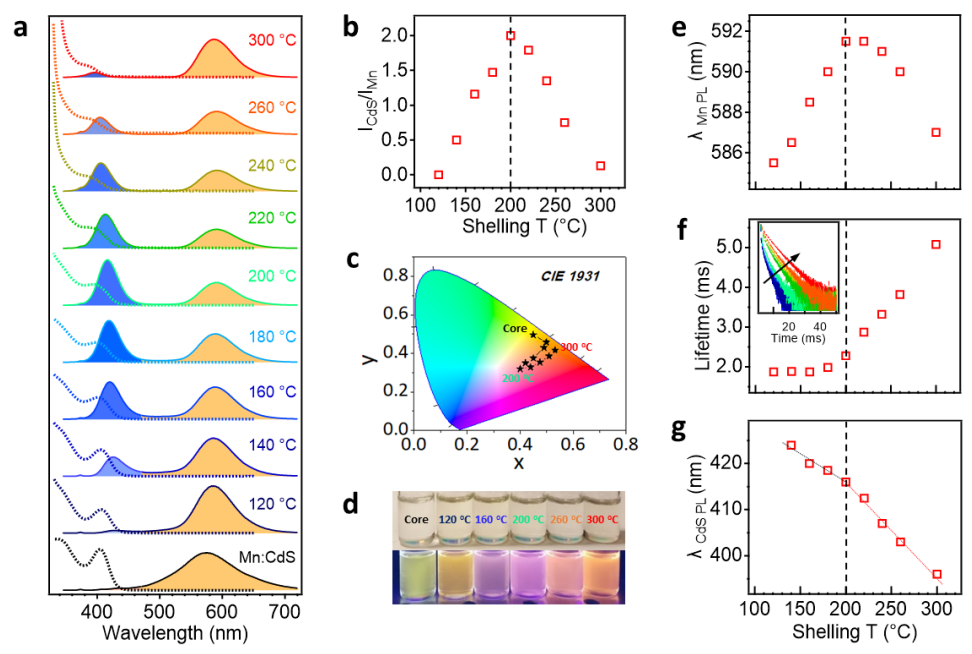
CdZnS lattice lead to the narrower linewidth of the Mn EPR peak (Figure 2b-2d) and less nonradiative decay of the Mn(II) excited state (See discussion on optical spectra below).

Figure 3a depicts the evolution of the absorption and photoluminescence (PL) spectra of the QDs during ZnS shell passivation, which clearly indicates three different stages of dopant behavior during shell passivation at different temperatures, including: I) initial surface dopant replacement; II) dopant migration below T<sub>b</sub>; and III) dopant ejection above T<sub>b</sub>. The first exciton absorption peak of the Mn:CdS is located at 406 nm with a single emission peak centered at ~580 nm attributed to the <sup>4</sup>T<sub>1</sub> to <sup>6</sup>A<sub>1</sub> transition of the Mn(II) ions, implying strong host-dopant coupling between the CdS host QDs and the dopants. In Stage I, a narrowing of the Mn(II) PL full width at half maxima (~ 70 nm) was observed as the shelling temperature reached 120 °C. When the sample reached 140 °C a second PL peak emerges at 424 nm which was identified as the CdS band-edge PL. Interestingly, a change in the relative intensities between the CdS and the Mn(II) PL was observed during the subsequent ZnS shell deposition. As the reaction temperature increases, the PL ratio increases from zero (at 120 °C) to a maxima value of 2.0 at T<sub>b</sub> (~ 200 °C) (Stage II), followed by a rapid decrease with a final PL ratio between CdS and Mn(II) reaching 0.13 at 300 °C (Stage III) (Figure 3b). The complete color change of the QDs from Stage I-III can be seen in the Commission International de l'Eclariage chromaticity coordinates (Figure 3c), as well as in the optical images of the samples under room and UV light (Figure 3d). The wide range of PL ratio of the doped core/shell QDs permits a fluorescent color scheme with great variability.

The energy transfer rate between the exciton and Mn ions can be interpreted quantitatively using the following equation 1:<sup>41</sup>

$$\frac{I_{Mn}}{I_{BG}} = n\Phi_{Mn} \frac{k_{ET}}{k_{UD-R}} \frac{\lambda_{BG}}{\lambda_{Mn}}$$
 (1)

Where  $I_{\rm Mn}$  and  $I_{\rm BG}$  are intensities of Mn emission and band-gap PL of the doped QDs, respectively; n is the number of Mn ions doped inside one QD;  $\lambda_{\rm BG}$  is the wavelength of the exciton emission,  $\lambda_{\rm Mn}$  is the wavelength of the Mn emission;  $\Phi_{\rm Mn}$  is the emission efficiency of a Mn ion,  $k_{\rm UD-R}$  is the radiative relaxation rate constant of an undoped QDs;  $k_{\rm ET}$  is the rate constant for the exciton to transfer its energy to a single Mn ions. Considering the small changes in the host and dopant PL position, as well as the same doping concentration below 260 °C, the energy transfer rate  $k_{\rm ET}$  between host QDs and Mn(II) is proportional to the PL ratio of Mn and host lattice ( $I_{\rm Mn}/I_{\rm BG}$ ). Since  $k_{\rm ET}$  is related to the overlap between the wavefunctions of exciton and Mn dopants, thus the distance between exciton and Mn ions. Therefore, the ratio of Mn(II) and QD emission reflects the degree of the energy transfer from QDs to Mn(II), and can be used as an optical "gauge" to monitor dopant sites inside the core/shell QDs. The tunable intensity ratio of the two emission bands of the doped QDs (Figure 3a and 3b), therefore, could be understood by the change in the H-D energy transfer efficiency.



**Figure 3**. Optical properties of Mn:CdS core and Mn:CdS/ZnS core/shell QDs. (a) Normalized optical absorption (dotted lines) and emission (solid lines) of Mn:CdS QDs and Mn:CdS/ZnS core/shell QDs, (b) PL intensity ratio of CdS and Mn, (c) the Commission International de l'Eclariage (CIE) chromaticity coordinates, (d) optical images of the samples under room (top) and UV (bottom) light, (e) the central of Mn(II) emission peak, (f) the derived Mn(II) PL lifetimes, and (g) the central of CdS PL peak of the Mn:CdS/ZnS QDs as a function of shelling temperature, inset shows the Mn(II) PL decay kinetics as a function of shelling temperature.

The increased PL ratio of CdS and Mn from 120 to 200 °C (Stage II, Figure 3b) indicates weakening of the host-dopant energy transfer (k<sub>ET</sub>), which can be attributed to less wavefunction overlap between the host QDs and Mn dopants due to the dopant outward migration to the alloyed interface (Cd<sub>1-x</sub>Zn<sub>x</sub>S)., The Mn(II) ion migration towards the interface is thermodynamically favored to minimize the lattice stain<sup>38, 42</sup> caused by the large size difference (13%) between Cd(II) and Mn(II) and will not further migrate to the ZnS shell if the core/shell structure can be maintained.

While the dopant migration toward the alloyed interface below  $T_b$  leads to increased PL ratio of CdS to Mn, the PL ratio decreases at temperatures above 200 °C, indicating strengthened H-D coupling, which cannot be simply explained by dopant migration toward the interface or even the surface of the core/shell QDs. The strengthened H-D coupling at high temperature can be understood, however, by the global alloying of the core/shell QDs at T >  $T_b$ , which leads to the formation of alloyed QDs without a distinct boundary between core and shell. Therefore, the exciton of the host lattice could largely delocalize throughout the alloyed QDs and lead to stronger host-dopant coupling from the efficient overlap between the dopant and exciton wavefunctions. Meanwhile, faster Mn dopant diffusion and ejection can occur above  $T_b$ , which is evidenced by the decreased dopant concentration and Mn PL quantum yield (QY) at 300 °C. (Figure S9)

The temperature-dependent dopant behavior within the core/shell QDs can also be supported by the analysis of the Mn PL peak position (Figure 3e). Ithurria et al. have reported that the Mn PL can be used as a radial pressure gauge in core/shell QDs and additional pressure arising from shell passivation can induce a Mn PL red-shift using a spherically symmetric elastic continuum model.<sup>43</sup> The large red-shift in the Mn(II) PL from 575 to 583 nm upon shelling at 120 °C indicates the rapid decomposition and deposition of the ZnS precursor onto the core QDs. With increasing ZnS shell thickness in Stage II (T < T<sub>b</sub>), the Mn(II) emission peak continues to red-shift until it reaches a maximum wavelength of 591.5 nm at 200 °C, which is consistent with the increasing pressure from thicker ZnS shells.<sup>43</sup> For temperatures above T<sub>b</sub> in Stage III, however, a steady blue-shift of the Mn PL is observed, suggesting decreased pressure from the ZnS shell applied on the Mn ions as a result ofdopant diffusion towards the surface and ejection. In addition, the peak position of PL excitation (PLE) spectra (monitor the Mn PL peak maximum position) follows the same trend as absorption and PL spectra (Figure S10), which further confirms that the Mn PL originates from the energy transfer from the excited electrons generated in CdS/ZnS core/shell QDs (stage II) and alloyed QDs (stage III).

To further confirm that the temperature-dependent dopant migration and ejection behavior, we studied the Mn PL decay dynamics via time-resolved emission measurements. Figure 3f shows a slow increase in the Mn PL lifetime of Mn:CdS/ZnS core/shell QDs grown during Stage II, which is consistent with increased Mn-Mn distance within the core/shell QDs,  $^{3743}$  due to the relatively slow dopant migration toward the interface below  $T_b$ . However, a rapid increase in Mn PL decay lifetime, from 2.3 to 5.0 ms (Figure 3f, Figure S8, and Table S4) for the QDs grown in Stage III, indicates more isolated Mn centers from the reduction of the "concentration quenching" from short-range Mn-Mn interactions,  $^{44-45}$  which supports fast dopant diffusion and ejection under high thermal energy in the alloyed QDs above  $T_b$ . In addition, the formation of alloyed interface and alloyed QDs can be further evidenced by the blue-shift of the host lattice PL due to the incorporation of Zn ions into the CdS core in stages II and III (Figure 3g). Stage II presents a slight blue-shift (~7 nm) of the CdS PL with increasing reaction temperature, while stage III experiences a larger PL blue-shift (~20 nm) with a larger negative slope, – 0.20 nm/°C, compared with – 0.13 nm/°C in Stage II. The sudden increase in slope further supports that global alloying is initiated at ~ 200 °C for CdS/ZnS core/shell QDs.

## **Discussion**

The energy transfer between host QDs and Mn(II) dopants could be interpreted quantitatively using the PL ratio of the host and dopants without considering nonradiative relaxation. However, the host-dopant energy transfer might compete with defect levels and nonradiative relaxation pathways within the QDs. In doped QDs, the excited electron-hole pair could be mainly deactivated *via* three possible pathways:<sup>39</sup> 1) radiative recombination at the QDs band edge with the rate constant  $k_{\text{BG-NR}}$ ; 2) non-radiative recombination at the QD band edge with the rate constant  $k_{\text{BG-NR}}$ ; and 3) energy transfer to a Mn ion, with the rate constant  $n \times k_{\text{ET}}$ , where n is the number of Mn ions doped inside one QD. After the energy is transferred to a Mn ion, the excited Mn ion ( ${}^{4}T_{1}$ ) relaxes to its ground state ( ${}^{6}A_{1}$ ), either radiatively with the rate constant  $k_{\text{Mn-NR}}$ , or non-radiatively with the rate constant  $k_{\text{Mn-NR}}$ . Therefore, the efficiency of host-to-dopant energy transfer ( $\Phi_{\text{ET}}$ ) can be represented as equation 2:

$$\Phi_{\rm ET} = \frac{nk_{\rm ET}}{k_{\rm BG-R} + k_{\rm BG-NR} + nk_{\rm ET}} \tag{2}$$

To verify that the change of PL ratio between the host QDs and Mn is dominated by H-D coupling rather than the changes of the surface traps during ZnS coating, we performed a control experiment where undoped CdS/ZnS core/shell QDs were synthesized using the same shell coating procedure. It was found that the PL QYs of undoped CdS/ZnS QDs are similar to the total PL QYs of Mn:CdS/ZnS QDs from host bandgap PL and Mn PL at the same reaction temperatures (Figure S9). Interestingly, slightly higher total PL QYs in Mn:CdS/ZnS QDs compared with that of undoped CdS/ZnS QDs at most of the measured temperatures were observed, which could be attributed to the fast host-dopant energy transfer that can efficiently compete with nonradiative relaxation pathways. 39, 46 However, the difference in PL QYs between the corresponding doped and undoped core/shell QDs is less than 10%. Therefore, it is reasonable to assume similar nonradiative relaxation rates ( $k_{\text{BG-NR}}$ ) for the corresponding doped and undoped QDs grown at the same temperature. 19, 37, 39 During the ZnS shell passivation, at different temperatures, changes in QYs of the core/shell QDs could indicate different defect contributions and therefore nonradiative relaxation processes. However, it has been reported that the ratio between Mn PL and bandgap PL of Mn doped CdS/ZnS core/shell QDs didn't change after surface zinc stearate treatment to remove surface-trap states with higher PL QYs, indicating no significant change of local environment around Mn dopants or energy transfer rate from surface trap states. <sup>39</sup> Based on the above assumption, the efficiency of H-D energy transfer ( $\Phi_{ET}$ ) can be roughly estimated by a flowing equation using steady-state approximation:<sup>39</sup>

$$\Phi_{ET} = 1 - \frac{QY_{BG}}{QY_{UD}} \approx \frac{QY_{Mn}}{QY_{UD}}$$
 (3)

Where the  $QY_{BG}$  and  $QY_{Mn}$  are the band-gap and Mn PL QY of doped QDs, respectively;  $QY_{UD}$  is the band-gap PL QY of the undoped QDs. We estimated the  $\Phi_{ET}$  by the ratio between Mn PL QY of doped QDs and PL QY of undoped NCs  $(QY_{Mn}/QY_{UD})$  using equation 3. It was found that  $\Phi_{ET}$  for the Mn:CdS/ZnS core/shell QDs decreased from 1.86 to 0.50 when the shelling temperature increased from 120 °C to 200 °C (Figure 4a). This result is consistent with the larger Mn-Mn distance due to the dopant migration toward the alloyed interface. However,  $\Phi_{ET}$  increases at  $T > T_b$  (Figure 4a), which indicates stronger host-dopant coupling after the formation of the globally alloyed QDs. The smaller final  $\Phi_{ET}$  of Mn:CdZnS alloyed QDs at 300 °C (1.02) compared with that of Mn:CdS/ZnS QDs initially formed at 120 °C (1.86) might be due to lower Mn concentrations as the result of high temperature dopant ejection as well as the near surface Mn doping in the alloyed QDs.

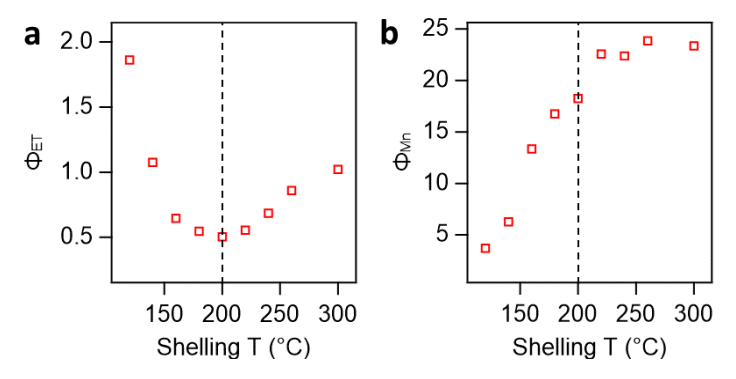


**Figure 4.** Energy transfer efficiency ( $\Phi_{ET}$ ) and Mn emission efficiency ( $\Phi_{Mn}$ ) calculated by Eq. 3 and 4 for doped QDs as a function of shelling temperature.

Based on the  $\Phi_{ET}$  data, we further calculated Mn emission efficiency ( $\Phi_{Mn}$ ). The  $\Phi_{Mn}$  is determined by the radiative rate constant  $k_{Mn-NR}$  and non-radiative rate constant  $k_{Mn-NR}$  as indicated by equation 4.

$$\Phi_{Mn} = \frac{k_{Mn-R}}{k_{Mn-R} + k_{Mn-NR}} = \frac{QY_{Mn}}{\Phi_{ET}}$$
(4)

 $k_{\text{Mn-R}}$  is a function of the dipole matrix element between the  ${}^{4}\text{T}_{1}$  and  ${}^{6}\text{A}_{1}$  states of the Mn dopants,  ${}^{17,\,39}$  which is not significantly affected by its local environment. However,  $k_{\text{Mn-NR}}$  depends on the micro-environment of Mn dopants and its local modes.  ${}^{39}$  Therefore,  $k_{\text{Mn-NR}}$  could change substantially with the Mn location in the QDs. Because of the anisotropic distortion of the Mn ligand coordinating environment from the 13% cationic size mismatch between Cd(II) and Mn(II) ions, the strain from the Mn incorporation inside CdS QDs would be larger compared with that of doped CdZnS alloyed lattice.  ${}^{19,\,38}$  The strain can lead to a larger  $k_{\text{Mn-NR}}$  and consequently a lower  $k_{\text{Mn-R}}$  of Mn:CdS/ZnS QDs.  ${}^{39}$  In contrast, less nonradiative decay of the Mn(II) excited state in Mn doped CdZnS alloyed QDs is expected because of reduced local strain on Mn dopant sites inside the alloyed lattice, which can provide dopant sites with smaller cationic size mismatch compared to that of CdS QDs. Based on Eq 4, smaller  $k_{\text{Mn-NR}}$  will lead to higher  $\Phi_{\text{Mn}}$ . Indeed, the  $\Phi_{\text{Mn}}$  of the doped core/shell QDs increased dramatically during the shell growth, which is consistent with the results from the narrowing of the EPR peaks with decreased local strain on Mn dopants during ZnS shell passivation (Figure 2b-2d) and can support the model of Mn(II) migration to the alloyed interface of CdS/ZnS core/ shell QDs in stage II as well as further ejection through the globally alloyed QDs in stage III.

It should also be noted that the defect concentration and crystallinity of the core/shell QDs might also be temperature-dependent. To further confirm that dopant behavior mainly depends on the temperature and local lattice composition, instead of crystallinity, we studied the thermal annealing effect on dopant behavior of the doped core/shell QDs grown below, at, and above  $T_b$  up to 4 hours (Figure 5a-c and Figure S11-12). Below the  $T_b$  (120 and 160 °C), the continuous increase in the CdS to Mn PL ratio and decreased H-D coupling was observed due to the outward dopant migration to the alloyed interface (Figure 5a and 5d). The core/shell QDs annealed at the  $T_b$  (200 °C) exhibit a nearly constant CdS to Mn PL ratio and Mn PL central peak position throughout the 4 hr annealing (Figure 5b and 5e), which indicates the same H-D coupling during the annealing process without further outward dopant migration. Once the core/shell QDs were annealed above the  $T_b$  (220, 240, and 300 °C, Figure 5c, 5f and Figure S11-12) a slight blue-shift in Mn peak position was observed, which is consistent with dopant ejection leading to less overall pressure being applied to Mn ions at  $T > T_b$ . In addition, a decreased PL ratio with more prominent Mn PL confirms the continued delocalization of the host exciton throughout the QDs, activating the Mn PL relaxation pathway, due to the global alloying.

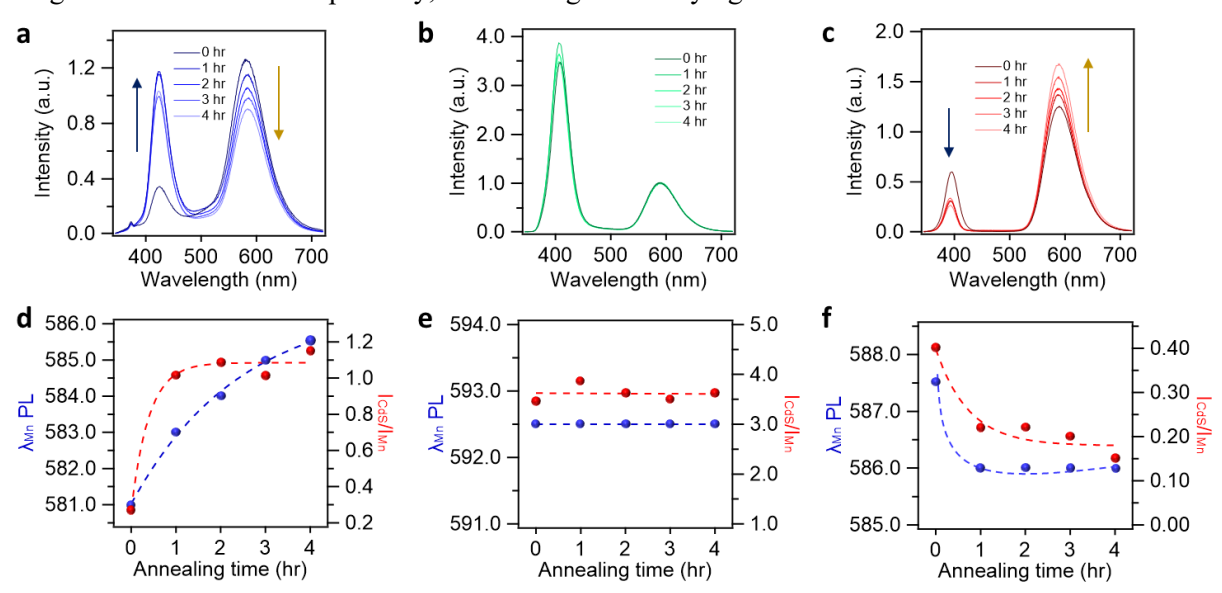
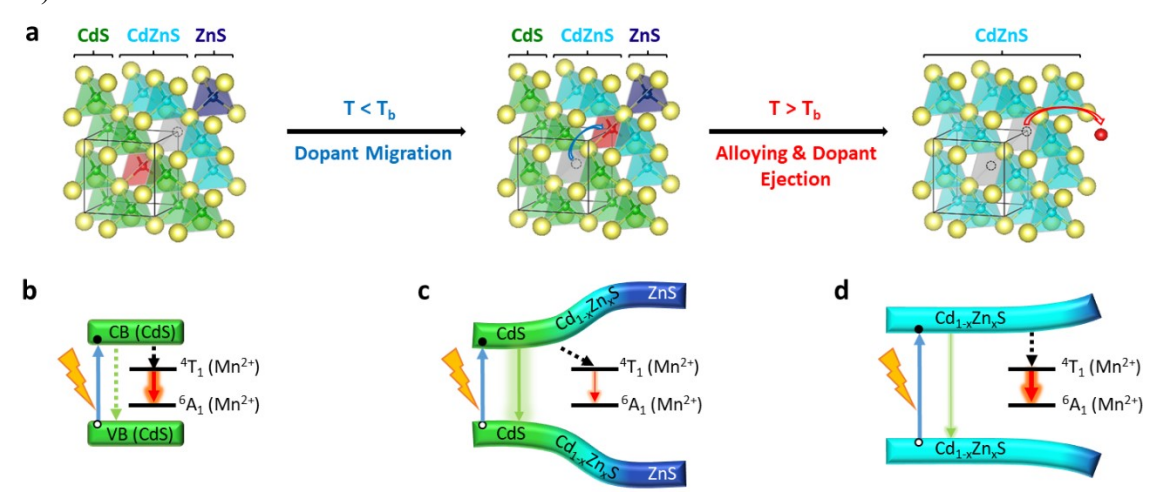


**Figure 5**. PL, Mn PL peak position, and PL intensity ratio of CdS and Mn of Mn:CdS/ZnS core/shell QDs annealed at 120 °C (e and h), 200 °C (f and i), and 300 °C (g and j) from 0 to 4 hrs.

The culmination of our data suggests that dopant migration in the presence of alloyed interface in core/shell QDs has a lower activation energy than dopant ejection and can occur at relatively low temperatures ( $T < T_b$ ) compared to dopant ejection due to self-purification ( $T > T_b$ ) (Scheme 1a). At  $T < T_b$ , the doped Mn ions can migrate toward a thin alloyed interface of the core/shell QDs, most likely mediated by cation vacancies, <sup>19, 47</sup> considering that half of the tetrahedral sites and all octahedral sites are empty in the cubic close packed S anions. The dopant migration leads to partial decoupling of CdS-Mn(II) host-dopant interaction with less energy transfer efficiency, therefore a new CdS PL can be observed in addition to Mn PL (Scheme 1c) compared with the sole Mn PL in Mn:CdS QDs (Scheme 1b). With sufficient thermal energy at  $T > T_b$ , global alloying of QDs can occur accompanied by dopant ejection (Figure 2a). The global alloying of the QDs results in a largely delocalized host exciton wavefunction and therefore strong host-dopant coupling with efficient energy transfer from host QDs to Mn dopants regardless of dopant location inside the QDs (Scheme 1d), leading to a more prominent Mn emission (Figure 3a).



**Scheme 1.** Temperature- and composition-dependent dopant migration and ejection inside Mn:CdS/ZnS QDs. (a) Schematic of temperature-dependent dopant migration, diffusion, and ejection within the CdS/ZnS cubic lattice. Tetrahedron in green, light blue, dark blue and red represent CdS, CdZnS, ZnS and MnS units, respectively. Illustrations of (b) core Mn:CdS QDs, (c) Mn:CdS/ZnS core/shell (below Tb) QDs, and (d) Mn:CdS/ZnS core/shell (above Tb) QDs energy levels and energy transfer diagrams (not to scale).

To further confirm the role of cationic size mismatch between dopants and micro-composition of host QDs, such as alloyed interface, we studied the dopant behavior in the Mn doped simple CdS QDs without adding the shell precursor during thermal annealing. It was found that there is no change in Mn doping environments at 140 °C, evidenced by the same optical, EPR data and doping concentration (Figure S13a and S15a). While only the loss of surface Mn can be observed when Mn:CdS QDs were annealed at 200 °C, evidenced by the narrowing of the Mn PL (Figure S13b and S14) and loss of the surface Mn EPR signal (Figure S15b), without further dopant migration and ejection, confirming the low activation energy of dopant migration in the presence of alloyed interface in the CdS/ZnS core/shell QDs. Furthermore, dopant ejection of Mn:CdS QDs without ZnS shell passivation can be observed at higher temperatures of 260 °C and above (Figure S13c-13d and 15c-15d), which is consistent with the higher thermal energy required for dopant ejection in core/shell QDs.

The thermodynamics of the dopant migration and ejection was also investigated computationally by evaluating the relative effective radial Helmholtz free energy  $\Delta A_{eff}(r)$  experienced by a Mn dopant ion inside a CdS/ZnS QD at lowest (120 °C) and highest temperatures (300 °C) from the experimental study (Figure 6). The core/shell QD with the stoichiometric formula of Cd<sub>288</sub>S<sub>288</sub>/Zn<sub>2488</sub>S<sub>2488</sub>, having a core radius of 1.5 nm and a core/shell radius of 3.0 nm was constructed from the bulk crystal structures. The  $\Delta A_{eff}(r)$  can provide key thermodynamic insight into effect of the core/shell interface on dopant ions and the experimentally observed temperature dependence of the dopant behaviors. The Helmholtz free energy is proportional to the logarithm of the configuration integral<sup>48</sup>

$$A(r,T) \propto -RT \ln[Z(r,T)]$$
 (5)

Using radial configuration integral Z(r,T), we define the change in the radial Helmholtz free energy  $\Delta A(r)$  as

$$\Delta A_{eff}(r) = A(r) - A(r_0) = -RT \ln \left[ \frac{Z(r,T)}{Z(r_0,T)} \right]$$
 (6)

where  $r_0$  is the reference point. The free energy barrier associate with the migration/ejection of the dopant was used to calculate the rate constant of the transitions using transition state theory as shown below:

$$k(T) = \frac{k_B T}{h} e^{-\Delta A^{\dagger}/k_B T} \tag{7}$$

where k(T) is the rate constant,  $\Delta A^{\dagger}$  is the free energy barrier along the transition path and h is the Planck's constant.

The calculated radial free energy for the movement of Mn dopants in CdS/ZnS QDs exhibits a local minimum at the core/shell interface of -0.111 eV at 300 °C (r = 1.5 nm, Figure S17a and Figure S16b). Therefore, the dopant migration from the interior of the core towards the core/shell interface can decrease the overall free energy. However, this decrease in the free energy is not monotonic and the minima at the core/shell interface is preceded by a free energy barrier within the CdS core (~4.25 \* 10<sup>-3</sup> eV at r = 0.8 nm at 573 K), which indicates that dopant migration still requires thermal activation (Figure 6a). The plot of the relative radial free energy also shows the presence of a much higher energy barrier with the height of 1.59 \* 10<sup>-2</sup> eV in the ZnS shell region (r = 1.5 - 3 nm, 573 K) for the dopant ejection to solvent minimum. The higher and broader barrier for dopant ejection (Stage III) than the dopant migration to the core/shell interface (Stage II) is consistent with fact that higher temperature required for dopant ejection than dopant migration observed in our experiments. The rate constant of for the dopant migration to the core/shell interface was found to be higher than the dopant ejection in CdS/ZnS QDs (Figure 6b, ~1.7 times higher at lower temperatures), demonstrating that dopant migration to interface is faster than Mn dopant ejection to solvent. This observation indicates that the presence of the core/shell interface has a positive impact of increasing the rate constant of the migration of the dopant from the core region.

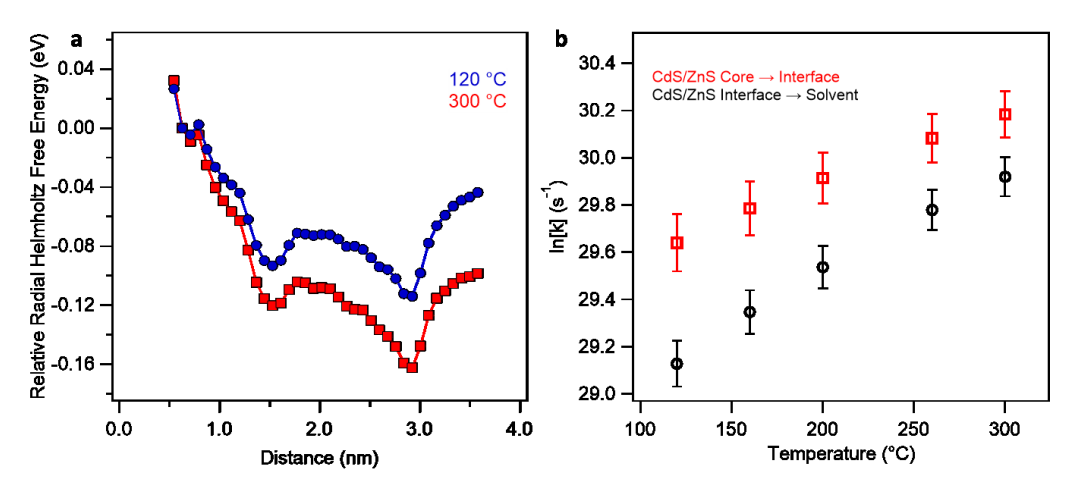


**Figure 6.** (a) The average relative free energy of the Mn(II) ion, quantum dot, and solvent system as the Mn(II) ion moves radial through CdS/ZnS at the lowest (120 °C) and highest (300 °C) temperature from the experimental study. (b) Rate constants of reactions for Mn(II) ion in both CdS/ZnS and CdS host lattice systems as a function of temperature.

# Conclusion

In summary, we have studied the mass transport of both dopants and host lattice in Mn:CdS/ZnS core/shell QDs. Three distinct stages of the mass transport can be resolved including: I) surface dopant replacement during the initial ZnS passivation; II) dopant migration toward the alloyed interface of CdS/ZnS core/shell QDs decreasing H-D coupling at  $T < T_b$ ; and III) global alloying of host QDs and dopant ejection re-strengthening H-D coupling at  $T > T_b$ . The dopant movement and location inside QDs, therefore the H-D coupling, is highly dependent upon the internal composition of the host QDs and temperature. The host lattice micro-compositionand temperature-dependent dopant behavior provides an efficient method to fine control the dopant arrangement,

and therefore the H-D interaction (decouple and couple) to continuously tune the properties of doped core/shell QDs.

## Methods

Chemicals. Cd(NO<sub>3</sub>)<sub>2</sub>·4H<sub>2</sub>O (≥99.0%, Sigma Aldrich), sulfur (99.998%, Sigma Aldrich), Mn(NO<sub>3</sub>)<sub>2</sub>·H<sub>2</sub>O (99.99%, Sigma Aldrich), oleylamine (OAm, 70% technical grade, Sigma Aldrich), 1-dodecanethiol (DDT, ≥98%, Sigma Aldrich), 1-octadecene (ODE, 90%, technical grade, Sigma Aldrich), zinc diethyldithiocarbamate (Zn(DDTC)<sub>2</sub>, 97%, Sigma Aldrich), ethanol (≥99.5%, VWR), and toluene (≥99.5%, EMD Chemicals) were used as received.

**Synthesis of Mn:CdS QDs.** Mn(II) doped CdS QDs were synthesized through a colloidal hot-injection technique as previously described.<sup>19</sup> Briefly, 41.2 mg (0.130 mmol) of Cd(NO<sub>3</sub>)<sub>2</sub>·4H<sub>2</sub>O, 5.82 mg (0.033 mmol) of Mn(NO<sub>3</sub>)<sub>2</sub>·H<sub>2</sub>O, 0.167 mL of DDT, and 10 mL of OAm were mixed in a three-neck flask. The mixture was degassed for 40 min at room temperature and another 10 min at 100 °C. The mixture was refilled with argon and kept at 110 °C for 30 min. Then, 0.667 mL of a 0.2 M solution of sulfur in OAm was swiftly injected into the flask at 160 °C. After the injection, the temperature was set at 120 °C and degassed for 10 min. The temperature was then raised to 240 °C for 5-10 min. The product was purified by adding toluene/ethanol.

ZnS Shell Growth for Mn:CdS/ZnS Core/Shell QDs. Mn:CdS/ZnS core/shell QDs were prepared using a single source shelling precursor (SSSP) method.<sup>34</sup> In a typical SSSP procedure, the premade Mn:CdS nanocrystals (3.0 nm diameter, 1 × 10<sup>-5</sup> mmol of particles, cleaned 3 times) in hexane were mixed with 490 mg of Zn(DDTC)<sub>2</sub> (a Zn and S containing precursor), 6.0 mL ODE, and 2.0 mL OAm in a 25 mL three-neck flask. The flask was then vacuumed at 70 °C for 1 h to remove excess air and hexane. The system was then flushed with Ar three times, and the reaction was brought to 300 °C at a ramping rate of 15 °C/min with sample being withdrawn every 20 °C.

Thermal annealing of Mn:CdS QDs and Mn:CdS/ZnS core/shell QDs. Thermal annealing of Mn:CdS QDs was conducted in the same solvents (OAm and ODE) and the same temperature profile as in the ZnS shell coating procedure but without adding Zn(DDTC)<sub>2</sub>. For thermal annealing of doped core/shell QDs at different temperatures, the QDs was cleaned twice to remove unreacted precursors, and redispersed in hexane and added to a solution of ODE and OAm, and the reaction was brought to the respective annealing temperature up to 4 hrs.

**Sample Characterizations.** Sample size, morphology, and dispersity were analyzed by transmission electron microscopy (TEM) using a FEI T12 Twin TEM operated at 120 kV with an LaB6 filament and Gatan Orius dual-scan CCD camera. Powder X-ray diffraction (XRD) patterns were taken on a Bruker D2 Phaser with a LYKXEYE 1-dimensional silicon strip detector using Cu K $\alpha$  radiation ( $\lambda$  =1.5406 Å).

Inductively coupled plasma-optical emission spectrometry (ICP-OES) analysis was performed on a PerkinElmer Optima 3300DV. Room temperature electron paramagnetic resonance (EPR) spectra were recorded at a microwave frequency of 9.4 GHz on a Bruker ELEXSYS- II E500 spectrometer. Absorption spectra were collected using an Agilent Cary 60 spectrophotometer. The PL measurements were conducted with a Horiba FluoroMax Plus spectrofluorometer. Time-resolved emission measurements were conducted using the time correlate single photon counting (TCSPC) on an Edinburgh FLS-980 spectrometer equipped with an  $\mu$ F2 60 W xenon flashlamp.

X-ray absorption fine structure (XAFS) analysis. XAFS experiments were performed at Sector 10 on the insertion device line. Pellet samples (pure materials/BN) were mounted 45° to the x-ray beam and measurements were performed in fluorescence using a Lytle detector. Calibrations were done on Cd(NO<sub>3</sub>)<sub>2</sub> powder or a Zn foil for the Cd and Zn edges, respectively.

XAFS data processing and analysis was done using the IFEFFIT suite of programs. A Hanning window was applied to a selected k-range (2-11 Å<sup>-1</sup>) to obtain the Fourier transformed extended XAFS (EXAFS) data. Using either the bulk ZnS or CdS lattice as our fitting model, FEFF6 was used to calculate the photoelectron scattering path amplitudes,  $F_i(k)$ , and phase,  $\phi(k)$ , and the samples were fit to the EXAFS equation,

$$\chi(k) = \frac{N_i S_o^2}{2kR_i^2} F_i(k) e^{-2k^2 \sigma_i^2} \sin\left[2kR_i + \phi_i(k)\right]$$
 (8)

which allowed for the extraction of pertinent information including the bond lengths ( $R_i$ ) and the EXAFS Debye-Waller factors (static disorders,  $\sigma_i^2$ ).

FEFF9 was used for the theoretical simulations of the Zn K-edge XANES spectra. <sup>49</sup> The calculations used the full multiple scattering approach considering cluster radii ranging from 2.5 to 5 Å, which corresponds to nearest neighbor up to next-next nearest neighbor scattering contributions. We first considered calculations of pure ZnS, where we investigate the effects that the nearest coordination shells have on the XANES spectra. In two calculations, Cd atoms were inserted for the Zn atoms into the next nearest neighbor and/or next-next nearest neighbor coordination shells to observe the effects of Cd incorporation on the ZnS Zn K-edge spectrum. For self-consistency, a 5 Å cluster was used and the effects of core hole was considered using the final state rule.

# Density functional theory (DFT) calculation.

Computational investigation of the Mn<sup>2+</sup> migration in the CdS/ZnS host lattice was performed at quantum mechanical level using density functional theory (DFT). The Q-CHEM electronic structure package<sup>50</sup> was used and the DFT calculation were performed using the B3LYP functional with LANL2DZ effective-core potential and basis set. The core/shell QD with the stoichiometric formula of Cd<sub>288</sub>S<sub>288</sub>/Zn<sub>2488</sub>, having a core radius of 1.5 nm and a dot radius of 3.0 nm was constructed from the bulk crystal structures.

To calculate  $\Delta A_{eff}(r)$ , we define the radial configuration integral Z(r,T) which is mathematically expressed as<sup>48</sup>

$$Z(r,T) = \int_{-\infty}^{+\infty} d\mathbf{r}' \exp\left[-\frac{U_{dopant-lattice}(\mathbf{r}')}{k_B T}\right] \delta(|\mathbf{r}'| - r)$$
(9)

where, T is temperature,  $k_B$  is Boltzmann constant.

Analysis of the quantum mechanics data revealed that the interaction of the  $Mn^{2+}$  with the host lattice can be predominantly described by a pairwise ion-dipole interaction potential as shown in Eq. (10),

$$U_{dopant-lattice}(r) = -\sum_{i} \frac{c}{|r_{dopant} - R_{i}^{lattice}|^{2}}$$
(10)

where  $\mathbf{R}^{\text{lattice}}$  is the center of the dipole,  $\mathbf{r}$  is the position of the dopant, and C is an adjustable parameter optimized to fit the DFT data. The integrals needed for calculating  $\Delta A_{\text{eff}}(r)$  were evaluated numerically using Monte Carlo sampling. Specifically,

$$\frac{Z(r)}{Z(r_0)} \approx \sum_{i=1}^{N_{Sample}} \frac{\exp\left[-\frac{U_{dopant-lattice}(r_{\tilde{1}}i)}{k_BT}\right]}{\sum_{i=1}^{N_{Sample}} \exp\left[\frac{U_{dopant-lattice}(r_{\tilde{0}}i_i)}{k_BT}\right]}$$
(11)

where,  $\{\hat{\mathbf{\eta}}_i\}$  is a set of unit vectors distributed randomly on a unit sphere. The vectors  $\{r\check{\mathbf{n}}_i\}$  uniformly sample points that are distance "r" from the center of the dot. For each value of the "r", a million randomly generated points were used for performing Monte Carlo sampling, this procedure was repeated for 10 additional runs to provide data to obtain averages for each temperature. The  $r_0$  for the Helmholtz free energy  $\Delta A_{eff}(r)$ , was selected at the local minima in the core region of the QD. The calculated values of the relative Helmholtz free energy  $\Delta A_{eff}(r)$  is presented in Figure S16 and S17 as a function of the dopant distance "r" from the center of the QD.

**Supporting Information.** The Supporting Information is available free of charge on the ACS Publications website.

Experimental details, all characterization data (XRD, TEM, XAFS, and EPR), optical data of the control experiments of Mn:CdS QDs and undoped CdS/ZnS core/shell QDs, thermal annealing data (optical and EPR), and computational analysis of Mn:CdS QDs and Mn:CdS/ZnS core/shell QDs (PDF)

# **Corresponding Author**

wzhen104@syr.edu

## **ORCID**

Weiwei Zheng: 0000-0003-1394-1806

Zhi-Jun Li: 0000-0002-2897-0450

Robert W. Meulenberg: 0000-0003-2696-8792

## **Notes**

The authors declare no competing financial interest

## ACKNOWLEDGMENT

W.Z. acknowledges support from the start-up grant of Syracuse University, ACS-PRF (# 59861-DNI5), and NSF CHE MSN (#05539CON04700). TEM measurements were performed at the Cornell Center for Materials Research (CCMR), which are supported through the NSF MRSEC program (DMR-1719875). We appreciate Dr. Boris Dzikovski and Dr. John Mark Franck for the assistance of EPR measurements. This work for ACERT was supported by the NIH grant NIH/NIBIB R010EB00315. The work at The University of Maine and Illinois Institute of Technology was supported by the NSF under Grant No. DMR-1708617. Materials Research Collaborative Access Team (MRCAT) operations are supported by the Department of Energy and the MRCAT member institutions. Portions of this research used resources of the Advanced Photon Source, a U.S. Department of Energy (DOE) Office of Science User Facility operated for the DOE Office of Science by Argonne National Laboratory under Contract No. DE-AC02-06CH11357.

## **REFERENCES**

- 1. Norris, D. J.; Efros, A. L.; Erwin, S. C., Doped nanocrystals. *Science* **2008**, *319* (5871), 1776-1779.
- 2. Erwin, S. C.; Zu, L. J.; Haftel, M. I.; Efros, A. L.; Kennedy, T. A.; Norris, D. J., Doping semiconductor nanocrystals. *Nature* **2005**, *436* (7047), 91-94.
- 3. Mocatta, D.; Cohen, G.; Schattner, J.; Millo, O.; Rabani, E.; Banin, U., Heavily Doped Semiconductor Nanocrystal Quantum Dots. *Science* **2011**, *332* (6025), 77-81.
- 4. Yu, J. H.; Liu, X.; Kweon, K. E.; Joo, J.; Park, J.; Ko, K. T.; Lee, D. W.; Shen, S.; Tivakornsasithorn, K.; Son, J. S.; Park, J. H.; Kim, Y. W.; Hwang, G. S.; Dobrowolska, M.; Furdyna, J. K.; Hyeon, T., Giant Zeeman splitting in nucleation-controlled doped CdSe:Mn2+ quantum nanoribbons. *Nat. Mater.* **2010**, *9* (1), 47-53.
- 5. Bryan, J. D.; Gamelin, D. R., Doped Semiconductor Nanocrystals: Synthesis, Characterization, Physical Properties, and Applications. In *Prog. Inorg. Chem.*, Karlin, K. D., Ed. 2005; Vol. 54, pp 47-126.
- 6. Beaulac, R.; Schneider, L.; Archer, P. I.; Bacher, G.; Gamelin, D. R., Light-Induced Spontaneous Magnetization in Doped Colloidal Quantum Dots. *Science* **2009**, *325* (5943), 973-976.
- 7. Zheng, W.; Strouse, G. F., Involvement of Carriers in the Size-Dependent Magnetic Exchange for Mn:CdSe Quantum Dots. *J. Am. Chem. Soc.* **2011**, *133* (19), 7482-7489.
- 8. Zheng, W.; Kumar, P.; Washington, A.; Wang, Z.; Dalal, N. S.; Strouse, G. F.; Singh, K., Quantum Phase Transition from Superparamagnetic to Quantum Superparamagnetic State in Ultrasmall Cd1–xCr(II)xSe Quantum Dots? *J. Am. Chem. Soc.* **2012**, *134* (4), 2172-2179.

- 9. Zandi, O.; Agrawal, A.; Shearer, A. B.; Reimnitz, L. C.; Dahlman, C. J.; Staller, C. M.; Milliron, D. J., Impacts of surface depletion on the plasmonic properties of doped semiconductor nanocrystals. *Nat. Mater.* **2018**, *17* (8), 710-717.
- 10. Pradhan, N.; Das Adhikari, S.; Nag, A.; Sarma, D. D., Luminescence, Plasmonic, and Magnetic Properties of Doped Semiconductor Nanocrystals. *Angew. Chem. Int. Ed.* **2017**, *56* (25), 7038-7054.
- 11. Knowles, K. E.; Hartstein, K. H.; Kilburn, T. B.; Marchioro, A.; Nelson, H. D.; Whitham, P. J.; Gamelin, D. R., Luminescent Colloidal Semiconductor Nanocrystals Containing Copper: Synthesis, Photophysics, and Applications. *Chem. Rev.* **2016**, *116* (18), 10820-10851.
- 12. McLaurin, E. J.; Vlaskin, V. A.; Gamelin, D. R., Water-Soluble Dual-Emitting Nanocrystals for Ratiometric Optical Thermometry. *J. Am. Chem. Soc.* **2011**, *133* (38), 14978-14980.
- 13. Beaulac, R.; Archer, P. I.; Ochsenbein, S. T.; Gamelin, D. R., Mn2+-Doped CdSe Quantum Dots: New Inorganic Materials for Spin-Electronics and Spin-Photonics. *Adv. Funct. Mater.* **2008**, *18* (24), 3873-3891.
- 14. Santra, P. K.; Kamat, P. V., Mn-Doped Quantum Dot Sensitized Solar Cells: A Strategy to Boost Efficiency over 5%. *J. Am. Chem. Soc.* **2012**, *134* (5), 2508-2511.
- 15. Li, Z.; Xiao, C.; Zhu, H.; Xie, Y., Defect Chemistry for Thermoelectric Materials. *J. Am. Chem. Soc.* **2016**, *138* (45), 14810-14819.
- 16. Wu, P.; Yan, X.-P., Doped quantum dots for chemo/biosensing and bioimaging. *Chem. Soc. Rev.* **2013**, *42* (12), 5489-5521.
- 17. Yang, Y.; Chen, O.; Angerhofer, A.; Cao, Y. C., On Doping CdS/ZnS Core/Shell Nanocrystals with Mn. *J. Am. Chem. Soc.* **2008**, *130* (46), 15649-15661.
- 18. Yang, Y.; Chen, O.; Angerhofer, A.; Cao, Y. C., Radial-Position-Controlled Doping in CdS/ZnS Core/Shell Nanocrystals. *J. Am. Chem. Soc.* **2006**, *128* (38), 12428-12429.
- 19. Hofman, E.; Robinson, R. J.; Li, Z.-J.; Dzikovski, B.; Zheng, W., Controlled Dopant Migration in CdS/ZnS Core/Shell Quantum Dots. *J. Am. Chem. Soc.* **2017**, *139* (26), 8878-8885.
- 20. Lounis, S. D.; Runnerstrom, E. L.; Bergerud, A.; Nordlund, D.; Milliron, D. J., Influence of Dopant Distribution on the Plasmonic Properties of Indium Tin Oxide Nanocrystals. *J. Am. Chem. Soc.* **2014**, *136* (19), 7110-7116.
- 21. Staller, C. M.; Robinson, Z. L.; Agrawal, A.; Gibbs, S. L.; Greenberg, B. L.; Lounis, S. D.; Kortshagen, U. R.; Milliron, D. J., Tuning Nanocrystal Surface Depletion by Controlling Dopant Distribution as a Route Toward Enhanced Film Conductivity. *Nano Lett.* **2018**, *18* (5), 2870-2878.
- 22. Zheng, W.; Singh, K.; Wang, Z.; Wright, J. T.; van Tol, J.; Dalal, N. S.; Meulenberg, R. W.; Strouse, G. F., Evidence of a ZnCr2Se4 Spinel Inclusion at the Core of a Cr-Doped ZnSe Quantum Dot. *J. Am. Chem. Soc.* **2012**, *134* (12), 5577-5585.
- 23. Pradhan, N.; Goorskey, D.; Thessing, J.; Peng, X., An Alternative of CdSe Nanocrystal Emitters: Pure and Tunable Impurity Emissions in ZnSe Nanocrystals. *J. Am. Chem. Soc.* **2005**, *127* (50), 17586-17587.
- 24. Pradhan, N.; Peng, X., Efficient and Color-Tunable Mn-Doped ZnSe Nanocrystal Emitters: Control of Optical Performance via Greener Synthetic Chemistry. *J. Am. Chem. Soc.* **2007**, *129* (11), 3339-3347.
- 25. Viswanatha, R.; Brovelli, S.; Pandey, A.; Crooker, S. A.; Klimov, V. I., Copper-Doped Inverted Core/Shell Nanocrystals with "Permanent" Optically Active Holes. *Nano Lett.* **2011**, *11* (11), 4753-4758.
- 26. Mikulec, F. V.; Kuno, M.; Bennati, M.; Hall, D. A.; Griffin, R. G.; Bawendi, M. G., Organometallic Synthesis and Spectroscopic Characterization of Manganese-Doped CdSe Nanocrystals. *J. Am. Chem. Soc.* **2000**, *122* (11), 2532-2540.
- 27. Kato, F.; Kittilstved, K. R., Site-Specific Doping of Mn2+ in a CdS-Based Molecular Cluster. *Chem. Mater.* **2018**, *30* (14), 4720-4727.

- 28. Vlaskin, V. A.; Barrows, C. J.; Erickson, C. S.; Gamelin, D. R., Nanocrystal Diffusion Doping. *J. Am. Chem. Soc.* **2013**, *135* (38), 14380-14389.
- 29. Barrows, C. J.; Chakraborty, P.; Kornowske, L. M.; Gamelin, D. R., Tuning Equilibrium Compositions in Colloidal Cd1–xMnxSe Nanocrystals Using Diffusion Doping and Cation Exchange. *ACS Nano* **2016**, *10* (1), 910-918.
- 30. Buonsanti, R.; Milliron, D. J., Chemistry of Doped Colloidal Nanocrystals. *Chem. Mater.* **2013**, 25 (8), 1305-1317.
- 31. Chen, D.; Viswanatha, R.; Ong, G. L.; Xie, R.; Balasubramaninan, M.; Peng, X., Temperature Dependence of "Elementary Processes" in Doping Semiconductor Nanocrystals. *J. Am. Chem. Soc.* **2009**, *131* (26), 9333-9339.
- 32. Zu, L. J.; Norris, D. J.; Kennedy, T. A.; Erwin, S. C.; Efros, A. L., Impact of ripening on manganese-doped ZnSe nanocrystals. *Nano Lett.* **2006**, *6* (2), 334-340.
- 33. Dalpian, G. M.; Chelikowsky, J. R., Self-Purification in Semiconductor Nanocrystals. *Phys. Rev. Lett.* **2006**, *96* (22), 226802.
- 34. Chen, D.; Zhao, F.; Qi, H.; Rutherford, M.; Peng, X., Bright and Stable Purple/Blue Emitting CdS/ZnS Core/Shell Nanocrystals Grown by Thermal Cycling Using a Single-Source Precursor. *Chem. Mater.* **2010**, *22* (4), 1437-1444.
- 35. Zheng, W.; Wang, Z.; Wright, J.; Goundie, B.; Dalal, N. S.; Meulenberg, R. W.; Strouse, G. F., Probing the Local Site Environments in Mn:CdSe Quantum Dots. *J. Phys. Chem. C* **2011**, *115* (47), 23305-23314.
- 36. Zheng, W.; Wang, Z.; van Tol, J.; Dalal, N. S.; Strouse, G. F., Alloy Formation at the Tetrapod Core/Arm Interface. *Nano Lett.* **2012**, *12* (6), 3132-3137.
- 37. Li, Z.-J.; Hofman, E.; Blaker, A.; Davis, A. H.; Dzikovski, B.; Ma, D.-K.; Zheng, W., Interface Engineering of Mn-Doped ZnSe-Based Core/Shell Nanowires for Tunable Host–Dopant Coupling. *ACS Nano* **2017**, *11* (12), 12591-12600.
- 38. Nag, A.; Chakraborty, S.; Sarma, D. D., To Dope Mn2+ in a Semiconducting Nanocrystal. *J. Am. Chem. Soc.* **2008**, *130* (32), 10605-10611.
- 39. Yang, Y.; Chen, O.; Angerhofer, A.; Cao, Y. C., Radial-position-controlled doping of CdS/ZnS core/shell nanocrystals: surface effects and position-dependent properties. *Chem. Eur. J.* **2009**, *15* (13), 3186-3197.
- 40. Shannon, R., Revised effective ionic radii and systematic studies of interatomic distances in halides and chalcogenides. *Acta Crystallographica Section A* **1976,** *32* (5), 751-767.
- 41. Zu, L.; Norris, D. J.; Kennedy, T. A.; Erwin, S. C.; Efros, A. L., Impact of Ripening on Manganese-Doped ZnSe Nanocrystals. *Nano Lett.* **2006**, *6* (2), 334-340.
- 42. Liu, L.; Li, X.; Fan, Y.; Wang, C.; El-Toni, A. M.; Alhoshan, M. S.; Zhao, D.; Zhang, F., Elemental Migration in Core/Shell Structured Lanthanide Doped Nanoparticles. *Chem. Mater.* **2019**, *31* (15), 5608-5615.
- 43. Ithurria, S.; Guyot-Sionnest, P.; Mahler, B.; Dubertret, B., Mn2+ as a radial pressure gauge in colloidal core/shell nanocrystals. *Phys. Rev. Lett.* **2007**, *99* (26), 265501.
- 44. Wang, Z.; Meijerink, A., Concentration Quenching in Upconversion Nanocrystals. *J. Phys. Chem. C* **2018**, *122* (45), 26298-26306.
- 45. Li, Z.-J.; Hofman, E.; Davis, A. H.; Khammang, A.; Wright, J. T.; Dzikovski, B.; Meulenberg, R. W.; Zheng, W., Complete Dopant Substitution by Spinodal Decomposition in Mn-Doped Two-Dimensional CsPbCl3 Nanoplatelets. *Chem. Mater.* **2018**, *30* (18), 6400-6409.
- 46. Chen, H.-Y.; Maiti, S.; Son, D. H., Doping Location-Dependent Energy Transfer Dynamics in Mn-Doped CdS/ZnS Nanocrystals. *ACS Nano* **2012**, *6* (1), 583-591.
- 47. Chakraborty, P.; Jin, Y.; Barrows, C. J.; Dunham, S. T.; Gamelin, D. R., Kinetics of Isovalent (Cd2+) and Aliovalent (In3+) Cation Exchange in Cd1–xMnxSe Nanocrystals. *J. Am. Chem. Soc.* **2016,** *138* (39), 12885-12893.

- 48. McQuarrie, D. A., Statistical Mechanics. 1975.
- 49. Rehr, J. J.; Kas, J. J.; Vila, F. D.; Prange, M. P.; Jorissen, K., Parameter-free calculations of X-ray spectra with FEFF9. *Phys. Chem. Chem. Phys.* **2010**, *12* (21), 5503-5513.
- 50. Shao, Y.; Gan, Z.; Epifanovsky, E.; Gilbert, A. T. B.; Wormit, M.; Kussmann, J.; Lange, A. W.; Behn, A.; Deng, J.; Feng, X.; Ghosh, D.; Goldey, M.; Horn, P. R.; Jacobson, L. D.; Kaliman, I.; Khaliullin, R. Z.; Kuś, T.; Landau, A.; Liu, J.; Proynov, E. I.; Rhee, Y. M.; Richard, R. M.; Rohrdanz, M. A.; Steele, R. P.; Sundstrom, E. J.; Woodcock, H. L.; Zimmerman, P. M.; Zuev, D.; Albrecht, B.; Alguire, E.; Austin, B.; Beran, G. J. O.; Bernard, Y. A.; Berquist, E.; Brandhorst, K.; Bravaya, K. B.; Brown, S. T.; Casanova, D.; Chang, C.-M.; Chen, Y.; Chien, S. H.; Closser, K. D.; Crittenden, D. L.; Diedenhofen, M.; DiStasio, R. A.; Do, H.; Dutoi, A. D.; Edgar, R. G.; Fatehi, S.; Fusti-Molnar, L.; Ghysels, A.; Golubeva-Zadorozhnaya, A.; Gomes, J.; Hanson-Heine, M. W. D.; Harbach, P. H. P.; Hauser, A. W.; Hohenstein, E. G.; Holden, Z. C.; Jagau, T.-C.; Ji, H.; Kaduk, B.; Khistyaev, K.; Kim, J.; Kim, J.; King, R. A.; Klunzinger, P.; Kosenkov, D.; Kowalczyk, T.; Krauter, C. M.; Lao, K. U.; Laurent, A. D.; Lawler, K. V.; Levchenko, S. V.; Lin, C. Y.; Liu, F.; Livshits, E.; Lochan, R. C.; Luenser, A.; Manohar, P.; Manzer, S. F.; Mao, S.-P.; Mardirossian, N.; Marenich, A. V.; Maurer, S. A.; Mayhall, N. J.; Neuscamman, E.; Oana, C. M.; Olivares-Amaya, R.; O'Neill, D. P.; Parkhill, J. A.; Perrine, T. M.; Peverati, R.; Prociuk, A.; Rehn, D. R.; Rosta, E.; Russ, N. J.; Sharada, S. M.; Sharma, S.; Small, D. W.; Sodt, A.; Stein, T.; Stück, D.; Su, Y.-C.; Thom, A. J. W.; Tsuchimochi, T.; Vanovschi, V.; Vogt, L.; Vydrov, O.; Wang, T.; Watson, M. A.; Wenzel, J.; White, A.; Williams, C. F.; Yang, J.; Yeganeh, S.; Yost, S. R.; You, Z.-Q.; Zhang, I. Y.; Zhang, X.; Zhao, Y.; Brooks, B. R.; Chan, G. K. L.; Chipman, D. M.; Cramer, C. J.; Goddard, W. A.; Gordon, M. S.; Hehre, W. J.; Klamt, A.; Schaefer, H. F.; Schmidt, M. W.; Sherrill, C. D.; Truhlar, D. G.; Warshel, A.; Xu, X.; Aspuru-Guzik, A.; Baer, R.; Bell, A. T.; Besley, N. A.; Chai, J.-D.; Dreuw, A.; Dunietz, B. D.; Furlani, T. R.; Gwaltney, S. R.; Hsu, C.-P.; Jung, Y.; Kong, J.; Lambrecht, D. S.; Liang, W.; Ochsenfeld, C.; Rassolov, V. A.; Slipchenko, L. V.; Subotnik, J. E.; Van Voorhis, T.; Herbert, J. M.; Krylov, A. I.; Gill, P. M. W.; Head-Gordon, M., Advances in molecular quantum chemistry contained in the Q-Chem 4 program package. Mol. Phys. 2015, 113 (2), 184-215.

# TOC

